LBNL FORGE Project 3-2535 Milestone 8 Report

Don Vasco, Lawrence Berkeley National Laboratory, University of California, Berkeley, CA
Kang Wang, Formerly at UC Berkeley, Currently at EarthScope
Roland Bürgmann, UC Berkeley

I. Fiber Optic Distributed Strain Sensing (DSS) Data

1. Introduction

In geothermal production it is important to understand the existing stress field and the changes in the stress associated with field development. The stress field is a controlling factor in the development and properties of natural and stimulated fractures. Furthermore, changes in the stress field can lead to associated seismicity and the potential for felt earthquakes. It is difficult to estimate stresses directly and they are typically inferred from well tests and observed strain. In this task our goal is to incorporate observed strain data into the fully integrated models of the stimulations at the FORGE site.

2. Evaluation of the DSS data associated with the 2024 stimulation

The most promising geodetic data turned out to be strain observations acquired from a Distributed Strain Sensing (DSS) optical fiber cable in well 16B. Other sensors and observations at or near the surface were not sensitive enough to measure deformation signals from the stimulations, though they might be useful for monitoring operations such as full geothermal production (Feigl and Batzli 2018). However, the DSS cable was directly impacted by the fractures generated or stimulated by the operations in April 2024. For example, during the stimulation Stage 3R on April 3rd the fiber optical cable in well 16B recorded significant positive strain (extension along the fiber optic cable) at 9,750 feet, with minor strains both above and below this depth (Figure 1). To enhance the signal solely due to the injection, any pre-injection strain was removed from each time series. The highly localized strain is compatible with the arrival of a fracture at the observing well 16B. The small strain at 3.7 days at all depths is likely an artifact and not significant.

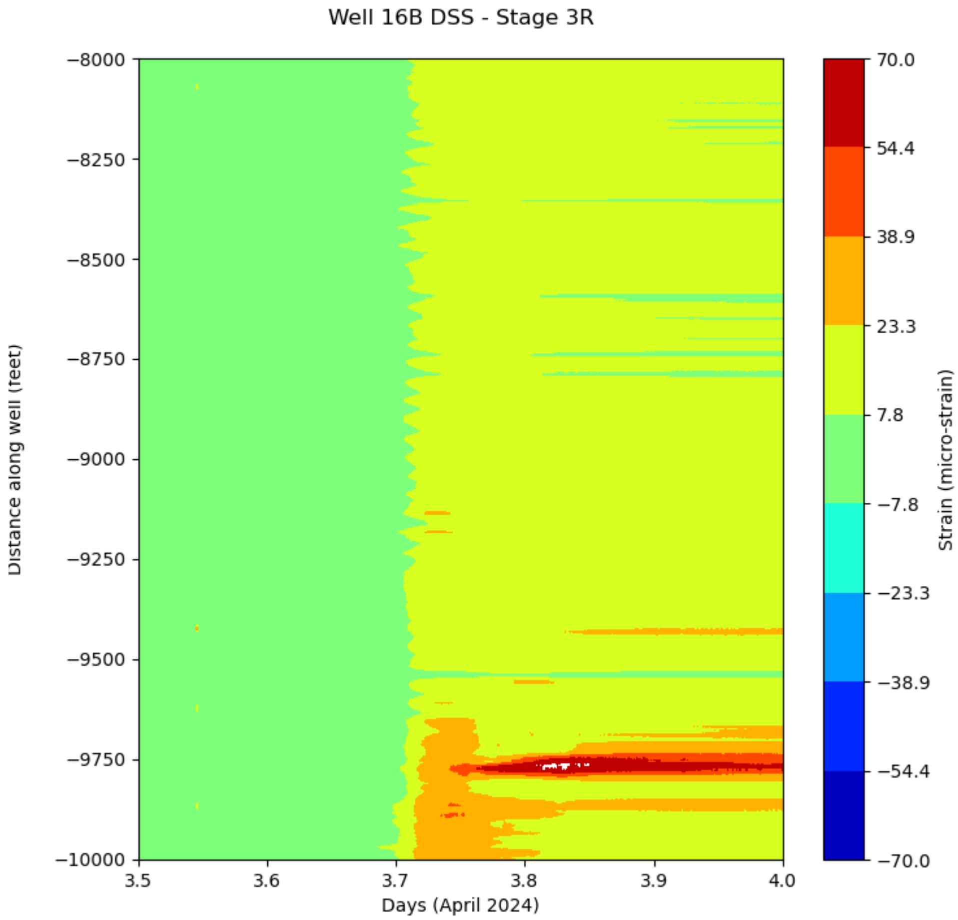

Figure 1. Distribute Strain Sensing data associated with Stage 3R on April 3rd, 2024.

The onset of major strain in well 16B, as shown in Figure 1, agrees with the timing of the fluid injection in well 16A (Figure 2), with a start time about 3.725 days. Note that the fracture is propped open due to the injection of the slurry. Thus, the strain remains even after the fluid pressure in the well is reduced to near zero.

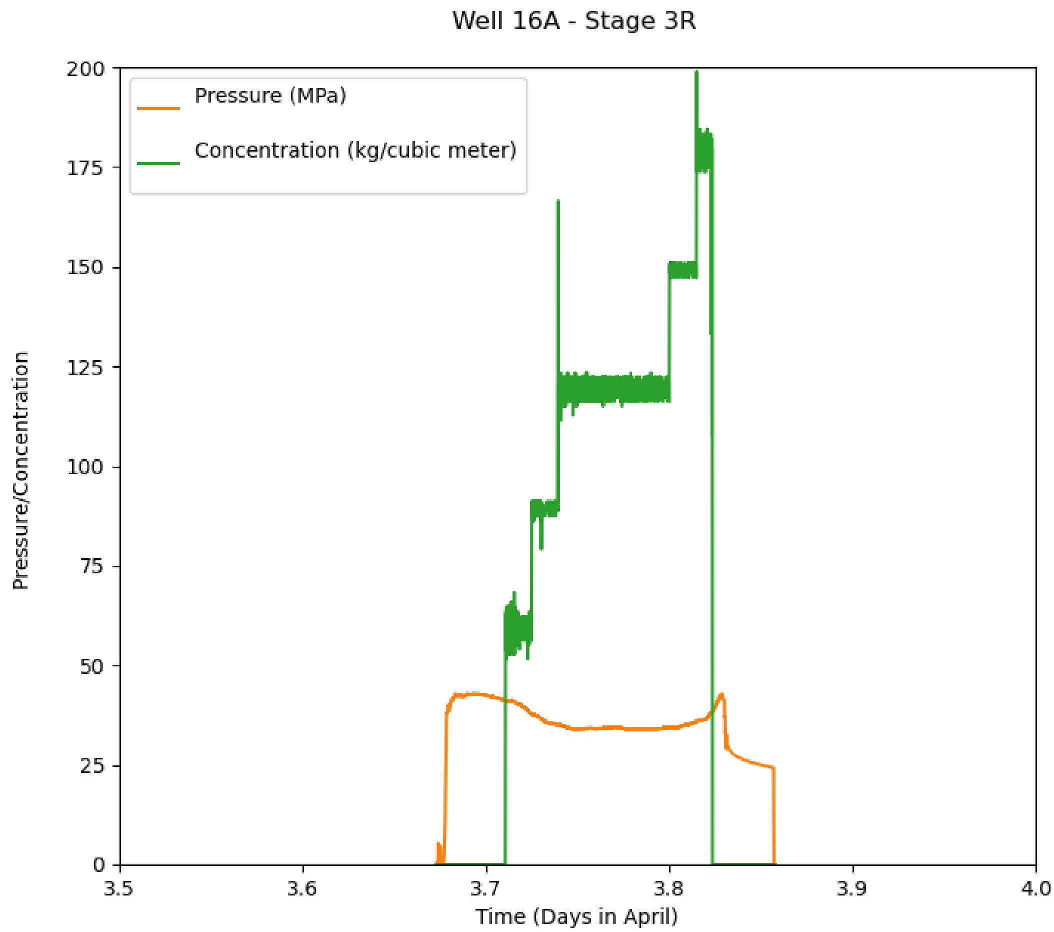

Figure 2. Pressure and proppant concentration during the Stage 3R stimulation.

We also evaluated several other intervals for DSS data quality, including observations from Stage 7, involving a stimulation on April 5th. The injection pressure and slurry rate during the stimulation are shown in Figure 3. The associated DSS data are shown in Figure 4. They are consistent with the opening of one or more fractures from an earlier stage as well as the stimulation of a fracture further up the well. As we shall see, the seismicity indicates that the fractures are primarily sub-vertical. The time of the strains seen during Stage 7 indicates opening of fractures deeper in the well, around the depth of those observed in Stage 3, followed by the arrival of fractures further up the well, around 9,500 feet, somewhat before 5.4 days.

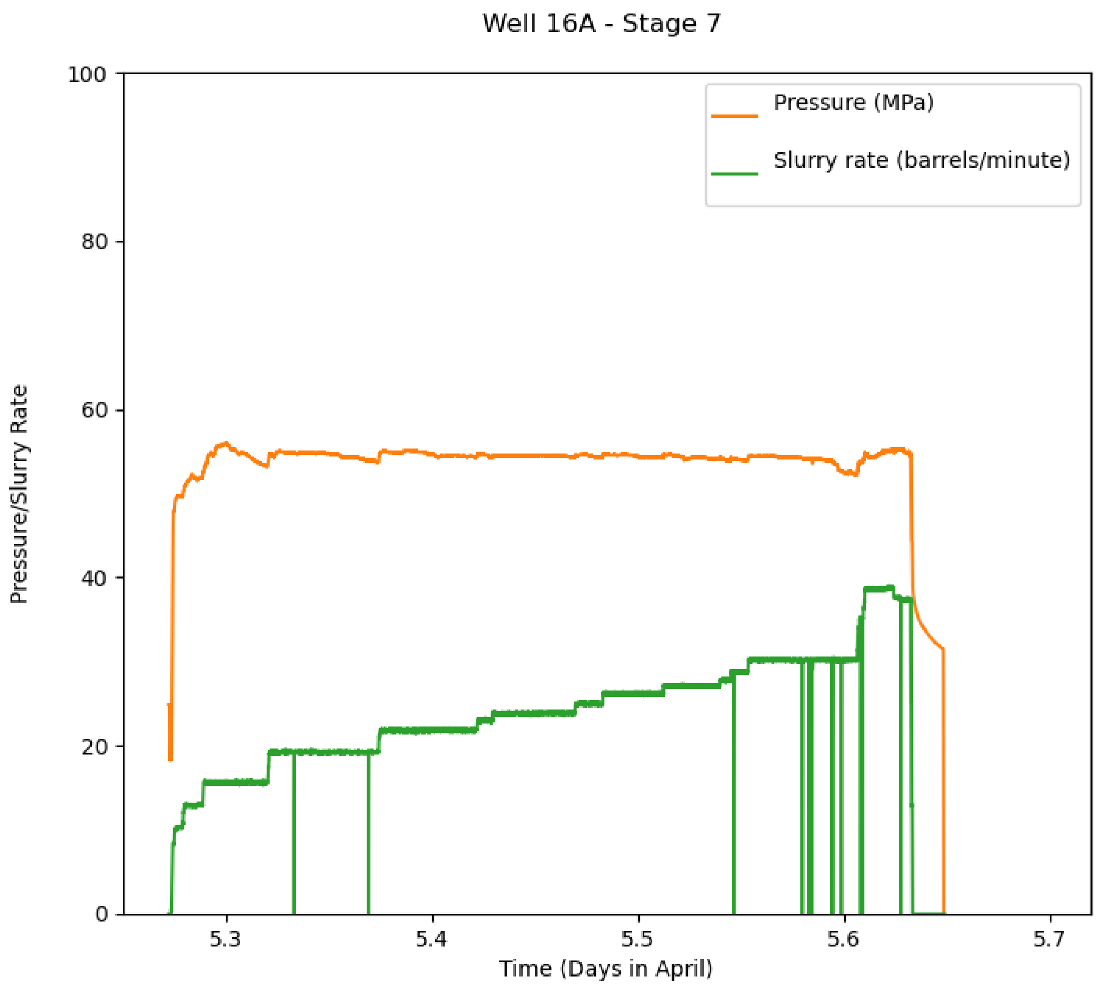

Figure 3. Pressure and slurry rate during the Stage 7 stimulation on April 5th.

Good quality DSS data are also associated with the later stages of the stimulations in April 2024. Figures 5 and 6 display the injected volume and DSS measurements for Stage 9. The pattern of strain indicates additional fractures stimulated within the interval of 8750 and 9000 feet of well 16B.

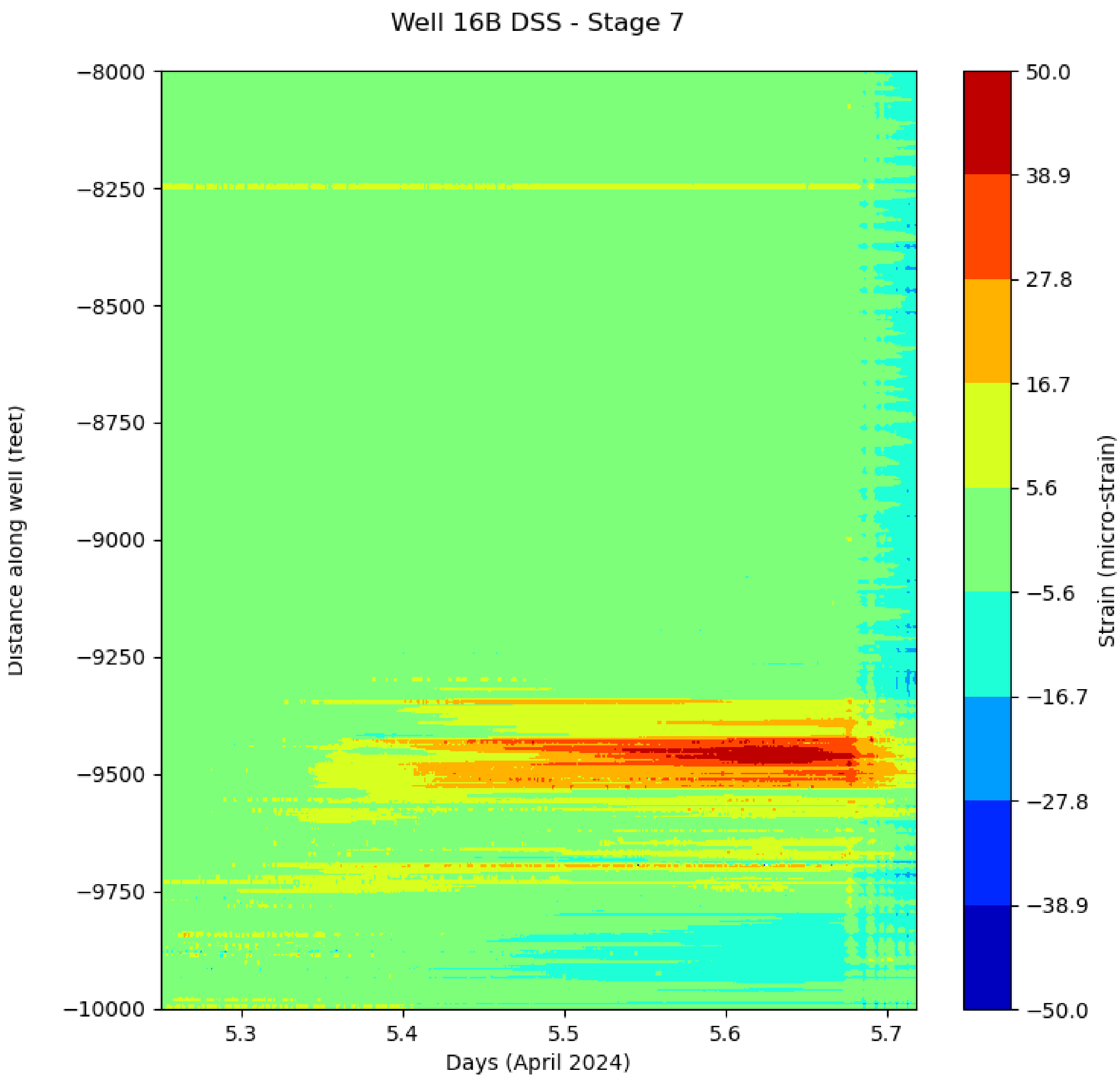

Figure 4. DSS measurements obtained during the Stage 7 stimulation.

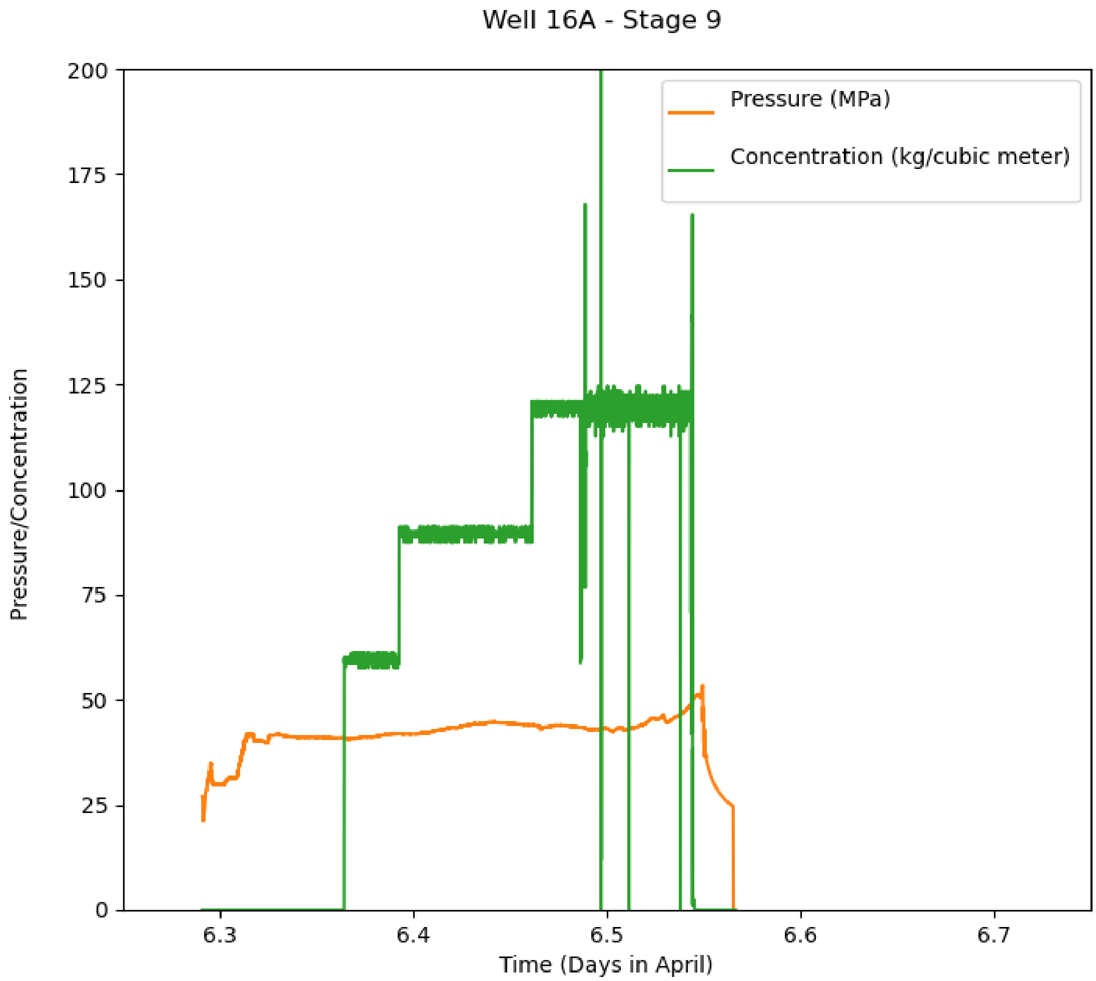

Figure 5. Pressure and proppant concentration as a function of time during the Stage 9 stimulation.

The injected volume and DSS observations for the final Stage 10, conducted on April 7th are shown in Figures 7 and 8, respectively. The stimulation seems to involve the activation of fractures in a similar interval of well 16B as those in Stage 9. The negative strain in well 16B above and below the fracture around 7.20 days (Figure 8) is compatible with the passage of the fracture and minor compression as the pressure decreases by a small amount and the fracture relaxes slightly.

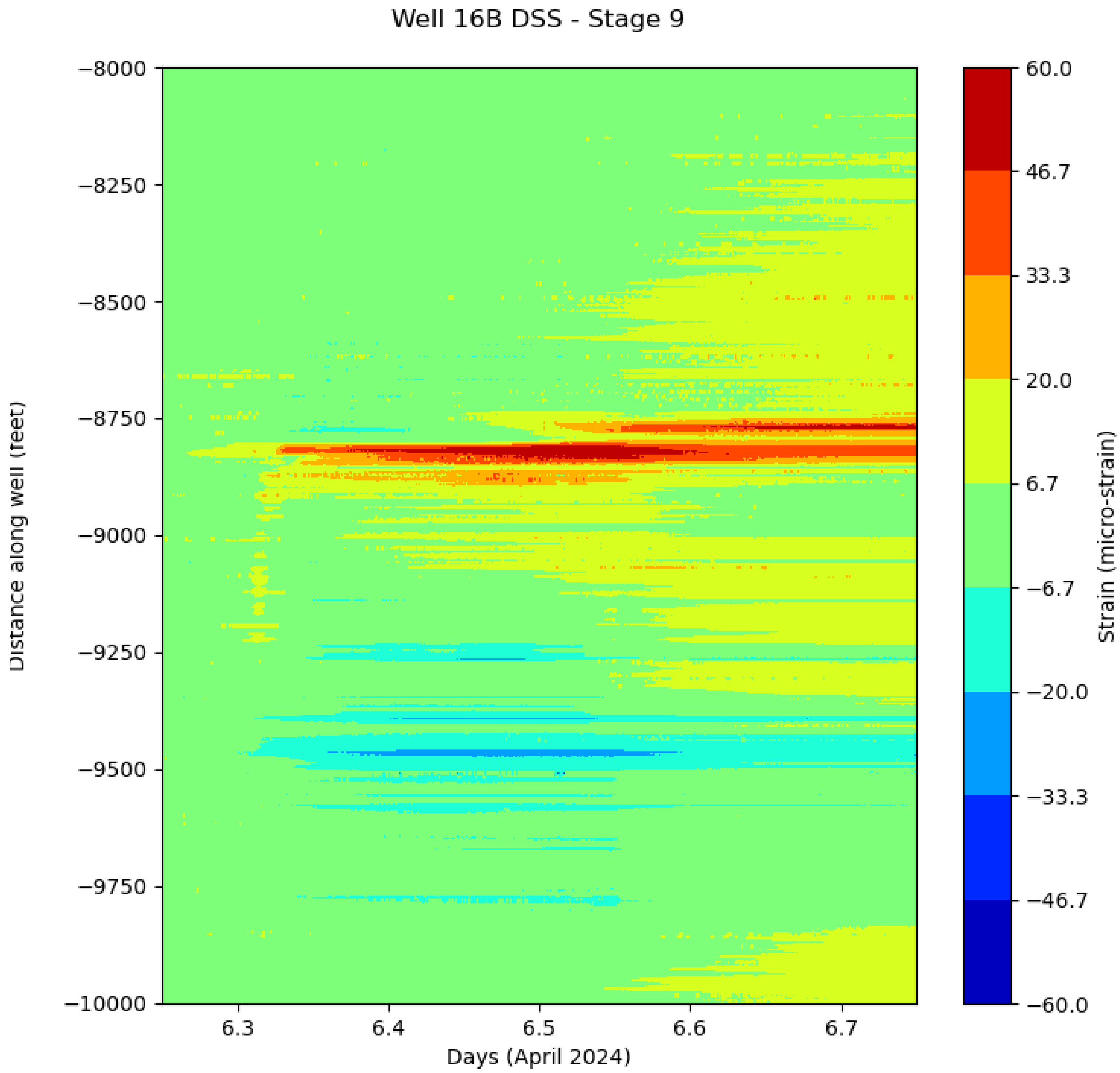

Figure 6. DSS observed in well 16B during the Stage 9 stimulation.

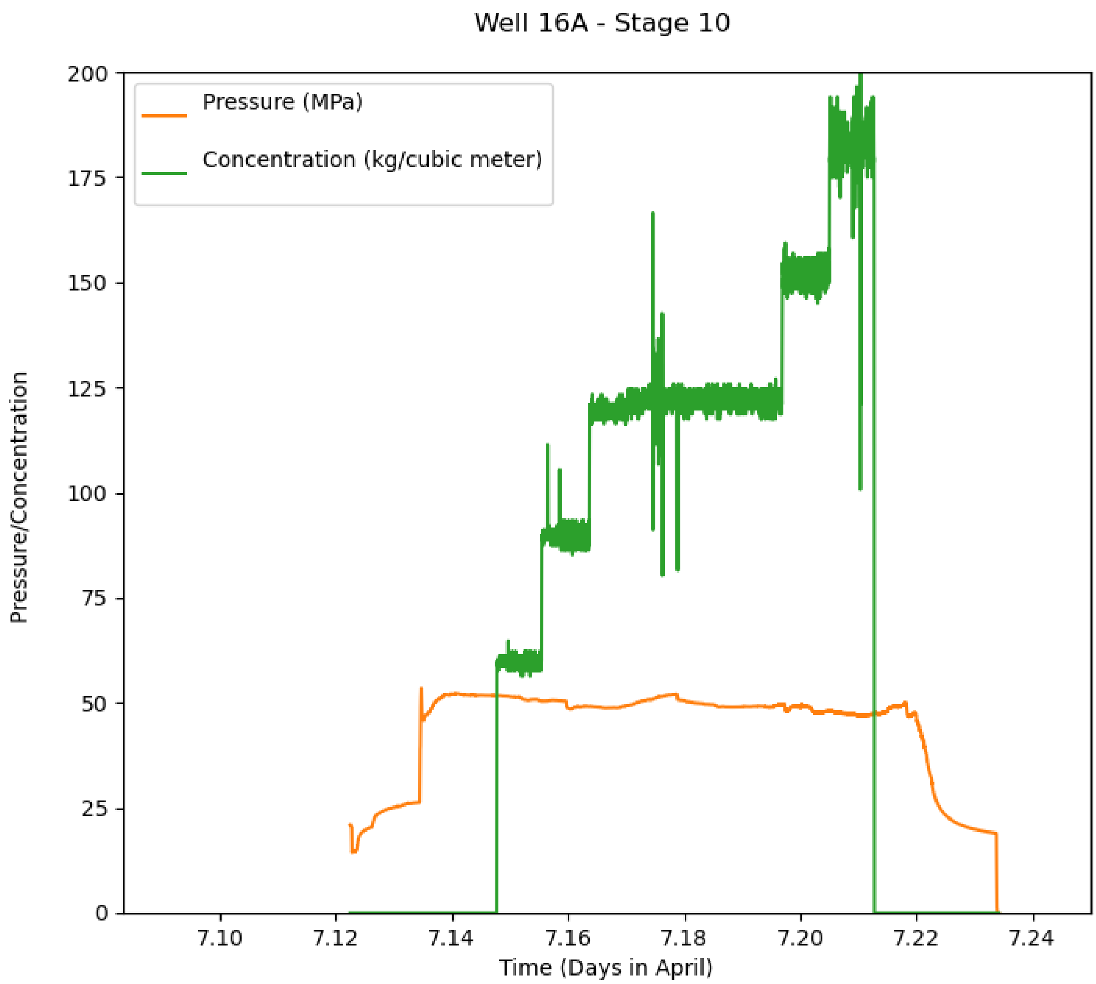

Figure 7. Pressure and proppant concentration during Stage 10.

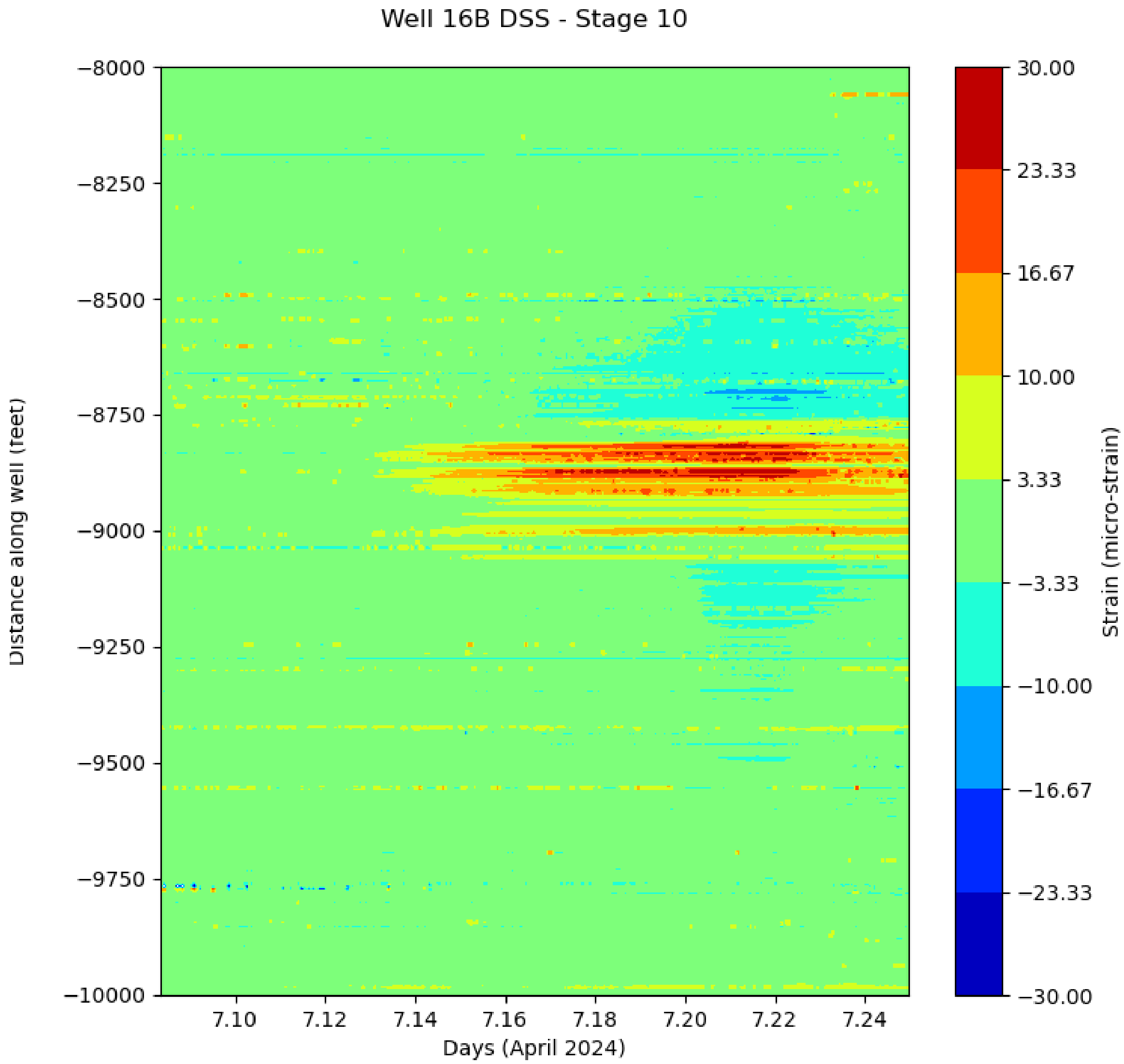

Figure 8. DSS observations in well 16B during Stage 10.

3. Correspondence Between DSS Observations and Microseismic Events

One objective of the project is to utilize both the DSS and the micro seismic data to better understand the evolving fracture geometry. The micro-seismicity for events during the stimulations in April 2024, as determined by Niemz et al. (2025), is shown in Figure 9.

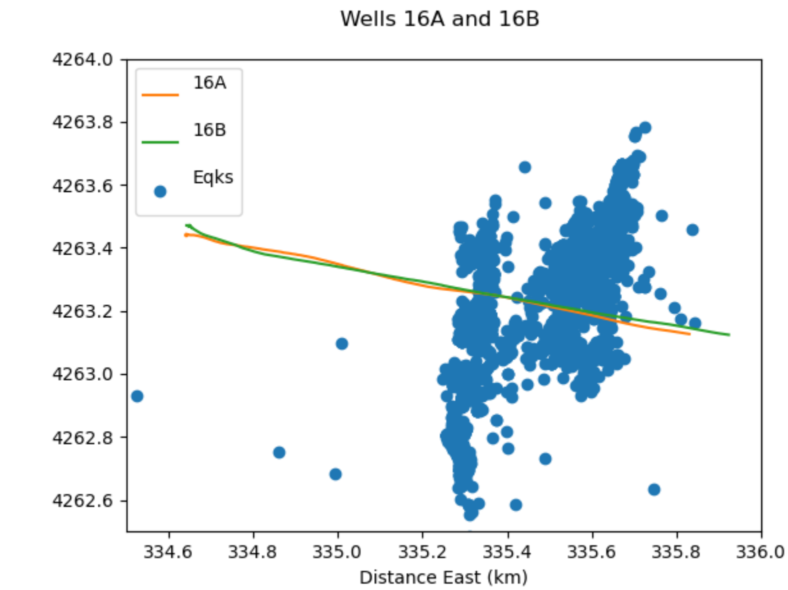

Figure 9. Microseismicity observed by Niemz et al. (2025) during the stimulations in April 2024 shown in map view. The two wells 16A and 16B are plotted as colored lines

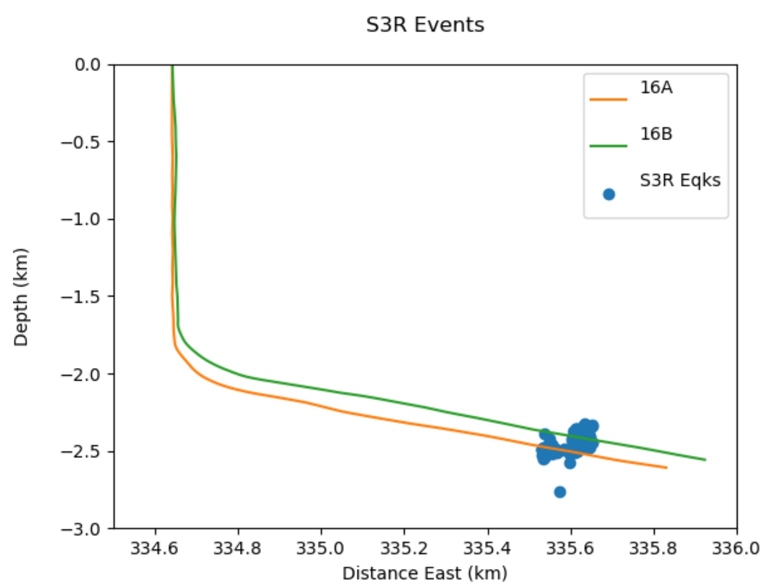

Figure 10. Microseismicity associated with Stage 3R.

A vertical view of the wells and the seismicity associated with Stage 3R are shown in Figure 10. The microseismicity observed during Stage 3R is plotted in Figure 11 on top of the DSS strain observed by the fiber optic cable in well 16B during this stage. The event time provides the horizontal position while the vertical position is obtained by finding the closest point of the well to the event and then using the distance of this point along the length of the well to give the vertical location. There is good agreement between the location of the maximum strain in well 16B and the location of the events along the well.

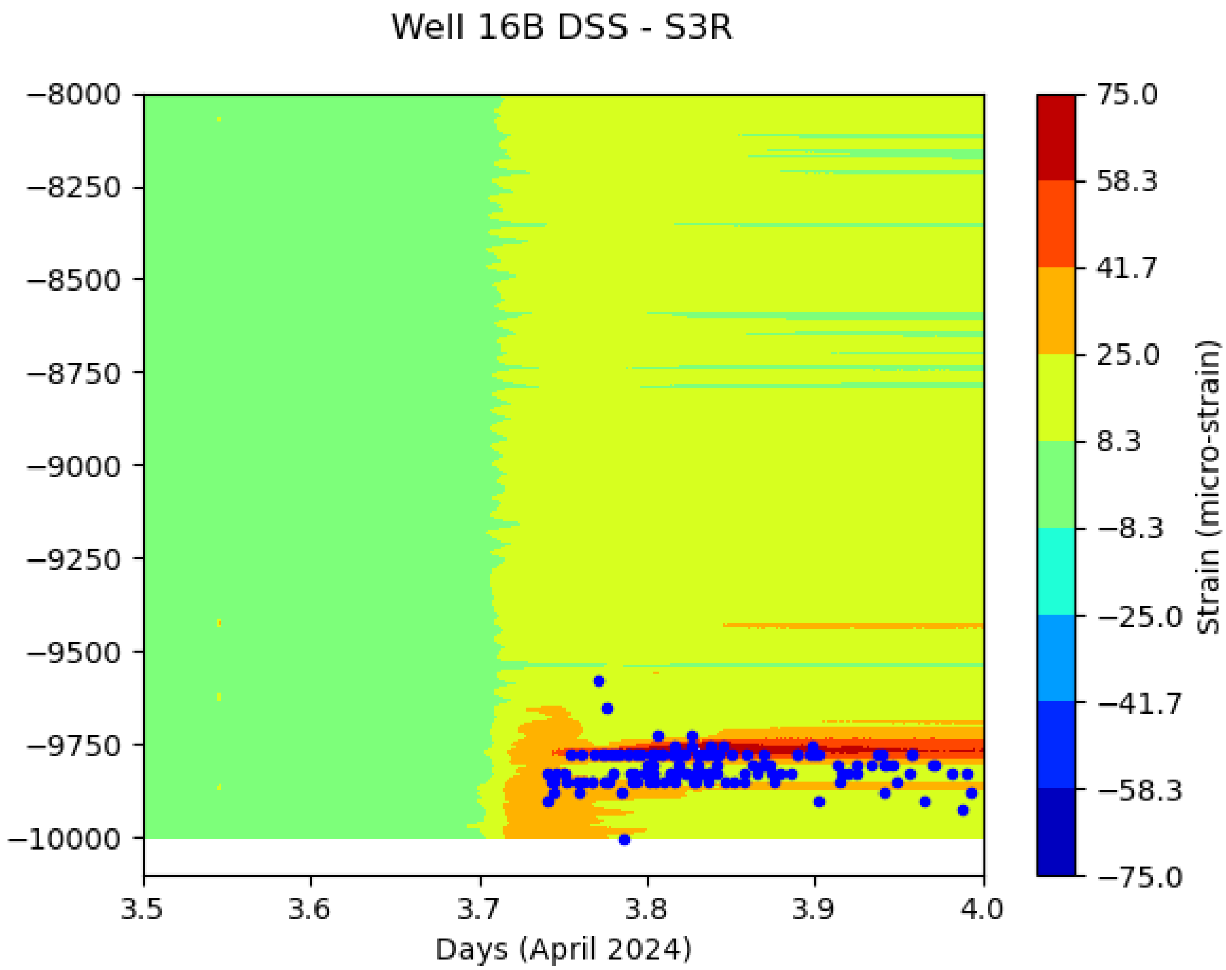

Figure 11. Plot of DSS data during Stage 3R and the seismicity observed during this stimulation. The vertical scale on the left is distance along the well in feet.

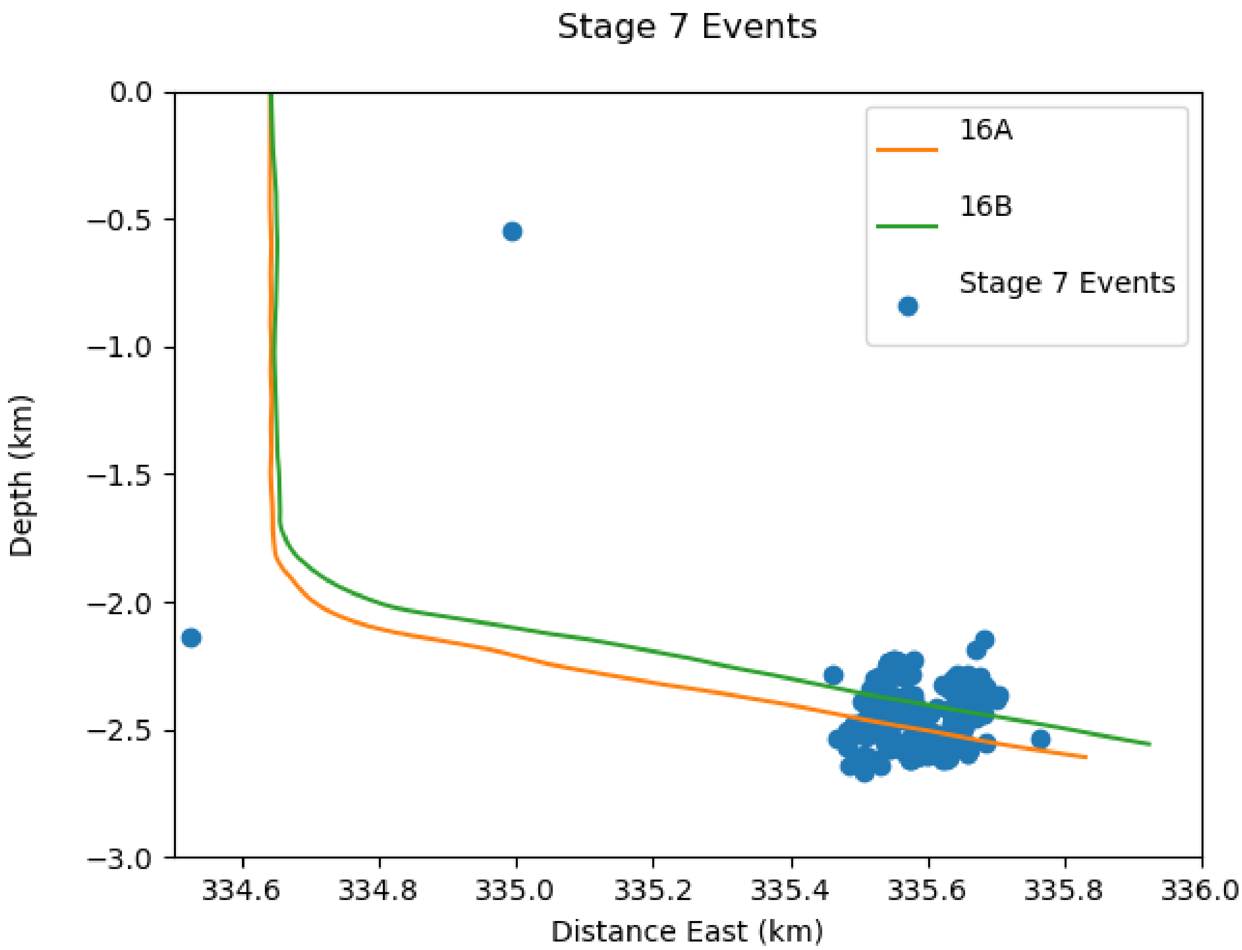

Figure 12. Seismicity corresponding to stimulation Stage 7.

A similar pair of plots for Stage 7 show a more diffuse pattern of seismicity for this later stage, perhaps due to the complexity introduced by the previous stimulations (Figures 12 and 13). The resulting pressure and temperature changes can induce complicated stress patterns.

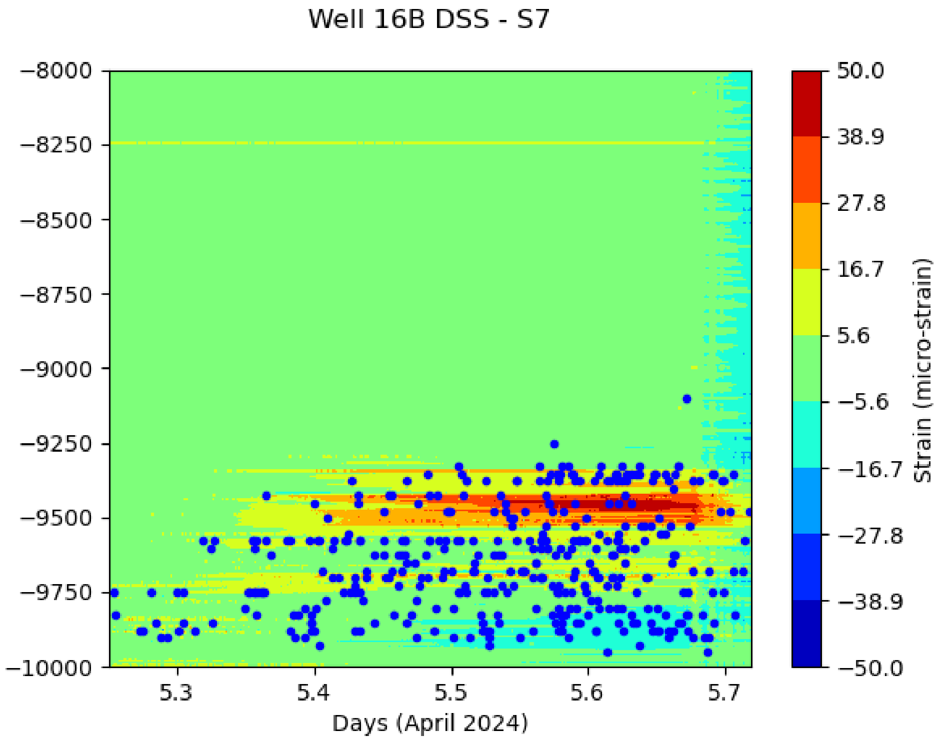

Figure 13. Seismicity plotted on top of strain in well 16B during Stage 7. The vertical scale on the left is distance along the well in feet.

Stages 9 and 10 also show a diffusive distribution of seismicity with concentrations near the regions of peak strains. Figures 14 and 15 display the seismicity locations and the correspondence between strain and seismicity respectively.

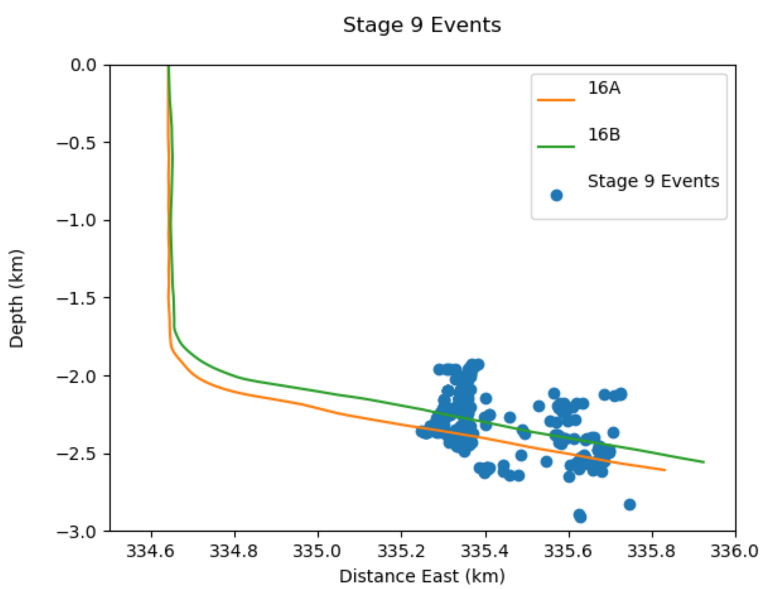

Figure 14. Vertical section with micro-seismic locations during Stage 9.

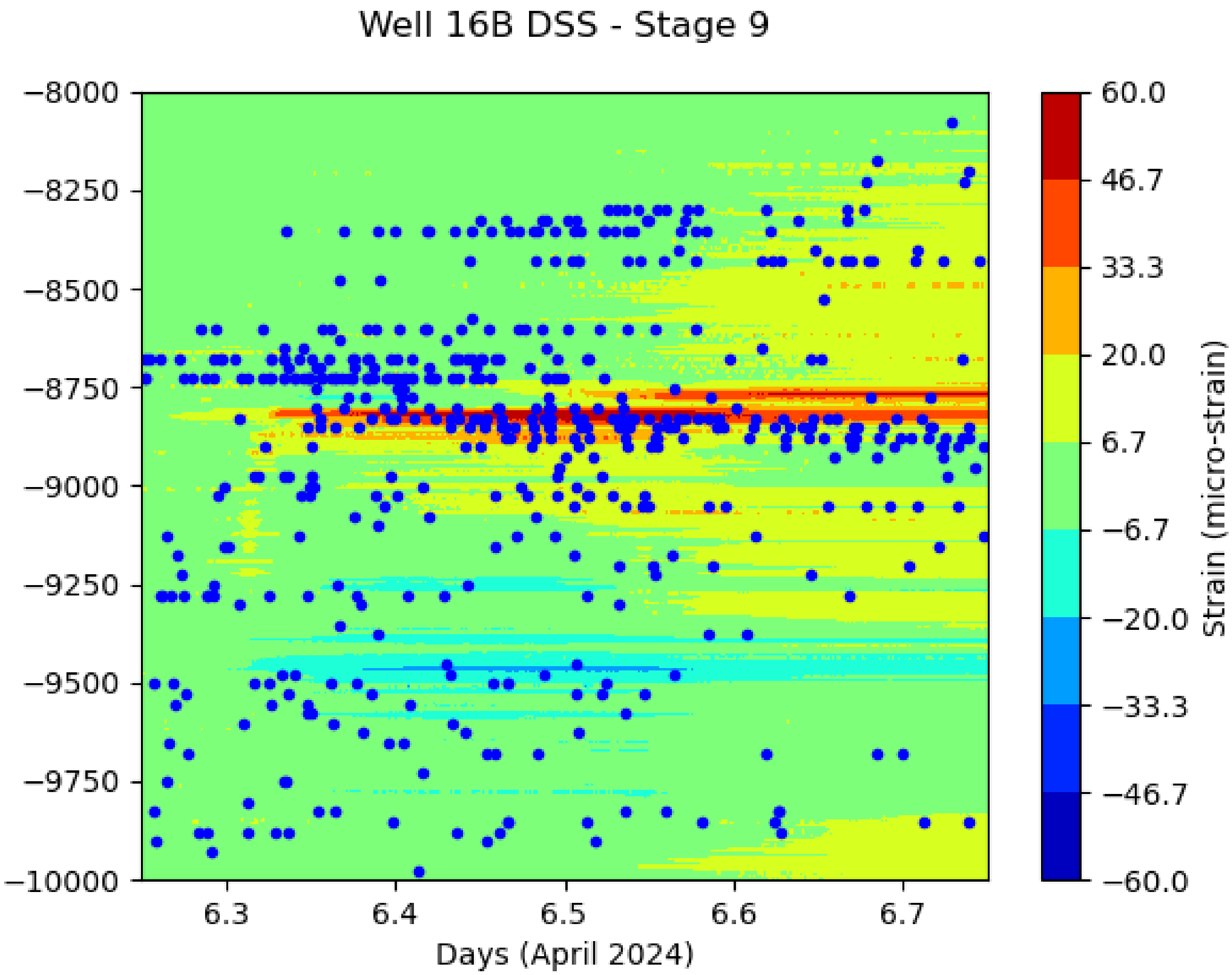

Figure 15. Seismicity plotted on top of strain in fiber optic cable in well 16b. The vertical scale on the left is distance along the well in feet.

Finally, we have the side view of seismicity and the correlation of seismicity and strain for Stage 10, shown in Figures 16 and 17. The area of slight compression in Figure 17 is mostly devoid of seismic events.

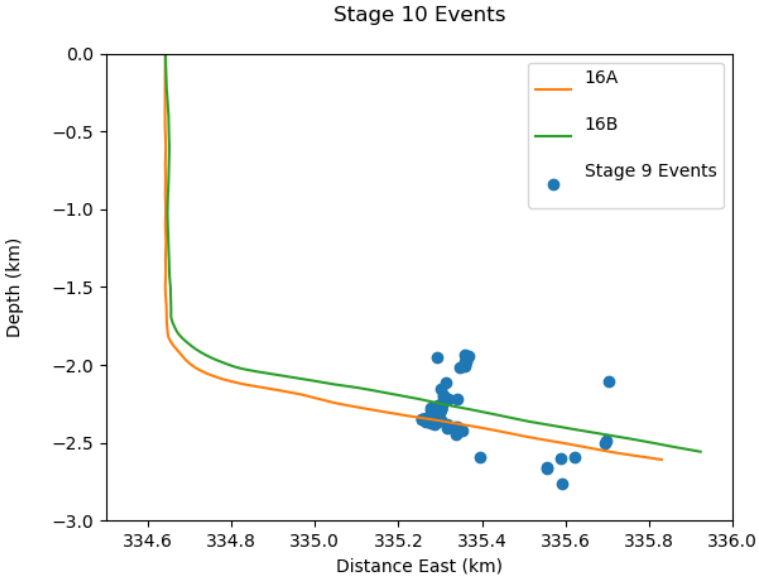

Figure 16. Vertical section showing seismicity generated during Stage 10.

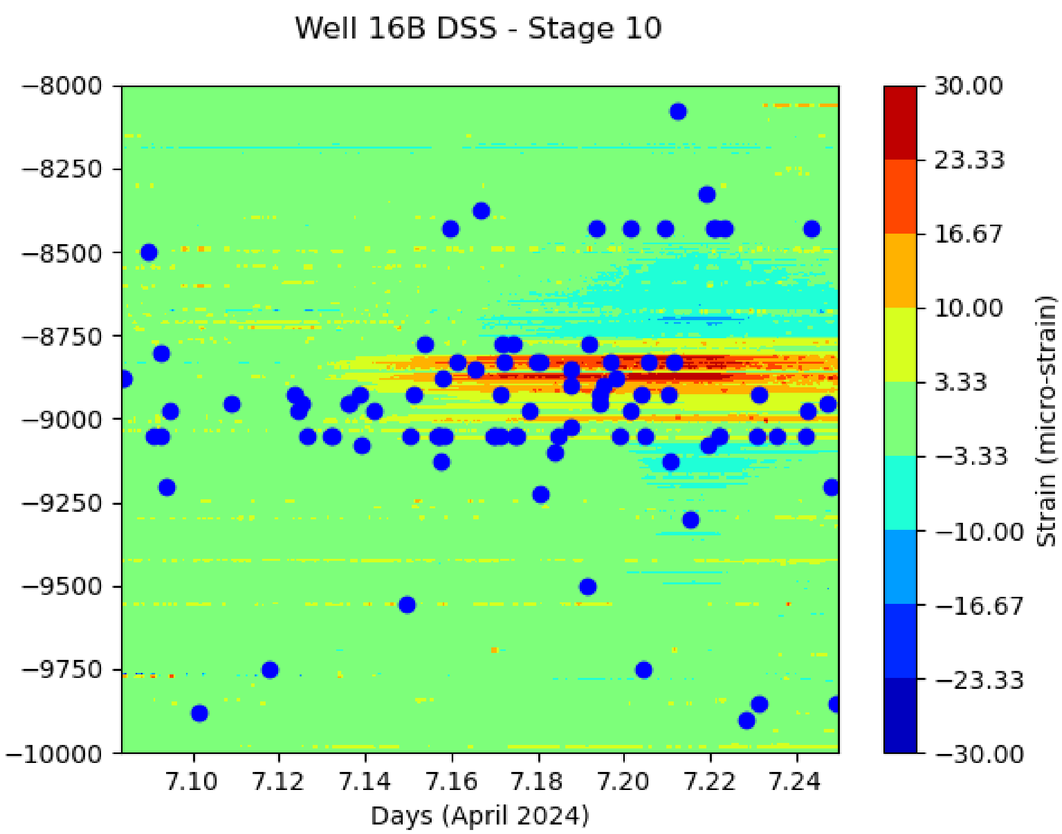

Figure 17. Correspondence between seismicity and strain in well 16B on April 7th during the Stage 10 stimulation. The vertical scale on the left is distance along the well in feet.

Overall, there seems to be a reasonable correspondence between the seismicity and the strain in well 16b. The best correlation appears to be for the first stimulation, Stage 3R. This makes intuitive sense, as this is the stage least influenced by any previous stimulations. The strain data from the fiber optic cable appear to be a valuable source of information on the fracture development during the stimulations in April 2024. The complexity suggests that further study and an integration of data sets is warranted.

4. Utilization of the Stimulation Related Deformation Data

The fiber optic strain data and seismicity will be used both to validate a coupled forward model

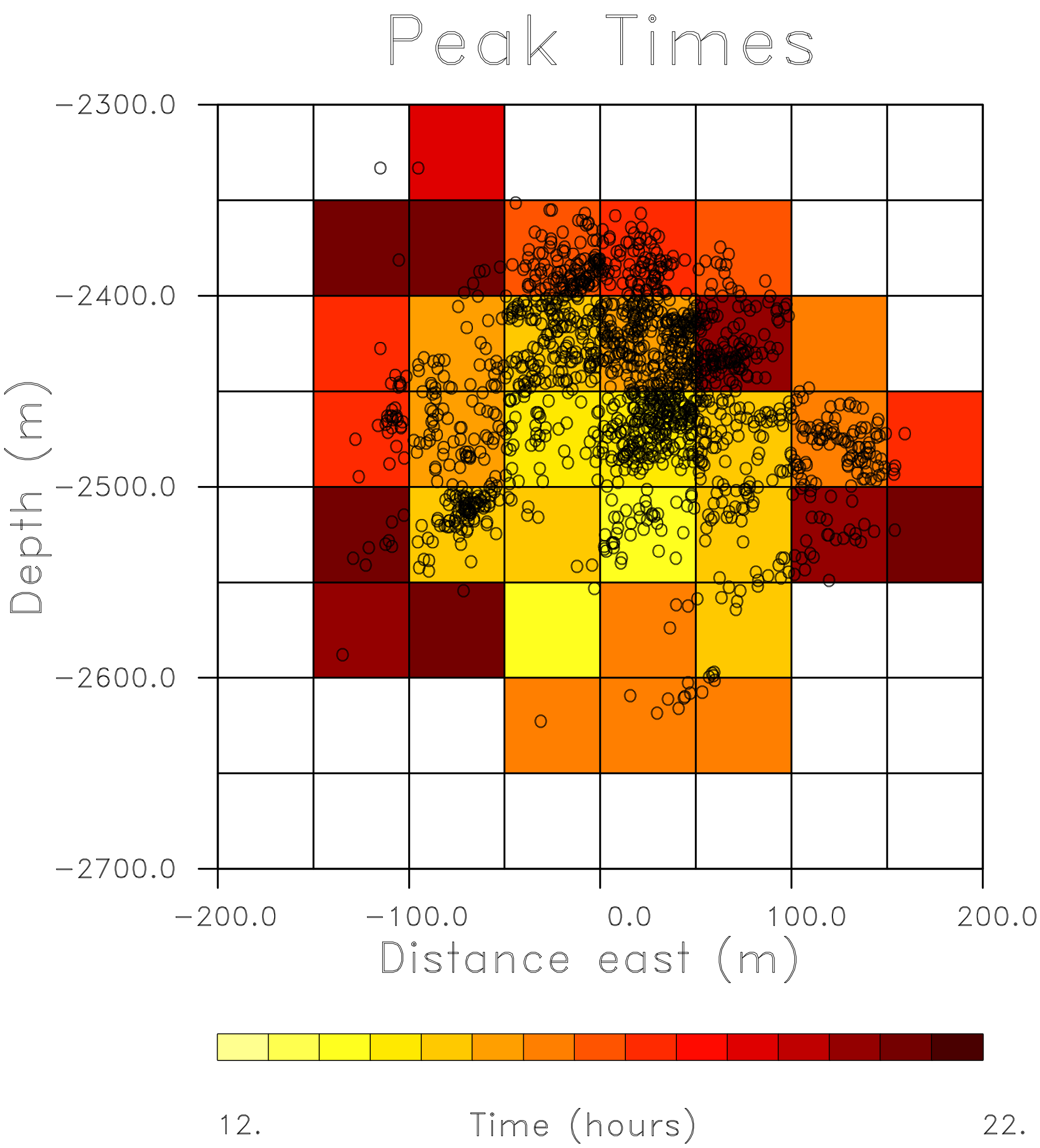

Figure 18. Hour at which peak seismicity was observed in various patches of a fracture model associated with the 3rd stimulation in April 2022 at the FORGE site.

and to invert for the fracture evolution during the stimulations. The observations will be used to develop conceptual models for the stimulated fractures that will be the basis of a numerical forward model. The inverse model will be a generalization of the work of Vasco et al. (2020), an inversion for the geometry of an evolving fracture in a poroelastic medium (Masson and Pride 2010). That approach, which only utilized the space-time variation of seismicity, will be generalized to include strain data, particularly DSS observations. As a preliminary application, the inversion method was applied to the time-varying seismicity for the April 2022 stimulations in well 16A. No DSS data was available for this inversion. The seismicity was used to define the area with aperture changes, the 'active' area of the fracture, using the rate- and state-dependent friction approach of Vasco et al (2020). The results of that inversion are shown in Figure 18. The evolution of the fracture is indicated by the time of peak seismicity.

II. Interferometric Synthetic Aperture Radar (InSAR) Data

1. Evaluation of InSAR data

We updated our previous Sentinel-1 InSAR analysis by incorporating additional data collected from 2019 to 2025. The FORGE site is covered by three satellite tracks: ASC100, DES93, and DES20. However, no further data were available along the two descending tracks (DES93 and DES20) after the end of 2021 (Figure 19). Consequently, we focused this effort on the ascending track ASC100.

Figure 20 shows the baseline distribution of images acquired along the ascending track ASC100 from 2019 to early 2025, along with the interferograms used to construct the surface displacement time series. To maintain relatively high radar coherence, we only generated interferograms using image pairs with temporal baselines of 36 days or less. We then applied the Small Baseline Subset (SBAS) method to estimate the average line-of-sight (LOS) velocity and surface displacement time series over the FORGE site.

Atmospheric noise is a major source of error in InSAR measurements. To mitigate atmospheric perturbations when solving for the average velocity field and displacement time series, we experimented with various methods, including the Common-Scene-Stacking technique (Tymofyeyeva and Fialko, 2015) and selected stacking (Wang et al., 2023). Despite these efforts the resulting velocity field and LOS displacement time series at individual points near the FORGE site remain relatively noisy (Figure 21). While the microseismic events are concentrated near the well ends of 16A and 16B, no distinct localized deformation signals are evident in the average LOS velocity map (Figure 6a). This suggests that any surface deformation induced by the stimulations is either below the InSAR detection threshold or obscured by atmospheric noise.

Since any surface deformation associated with the stimulations is expected to be small and localized, while atmospheric noise tends to be spatially correlated over small areas, we further reduced the noise by examining the relative displacement time series across pixels. Specifically, we compared pixels near the recorded microseismicity with pixels located approximately 1 km to the north. As anticipated, the relative displacement time series between these areas exhibit significantly reduced variation. However, no clear abrupt changes were observed in the relative LOS displacement time series during the stimulation tests.

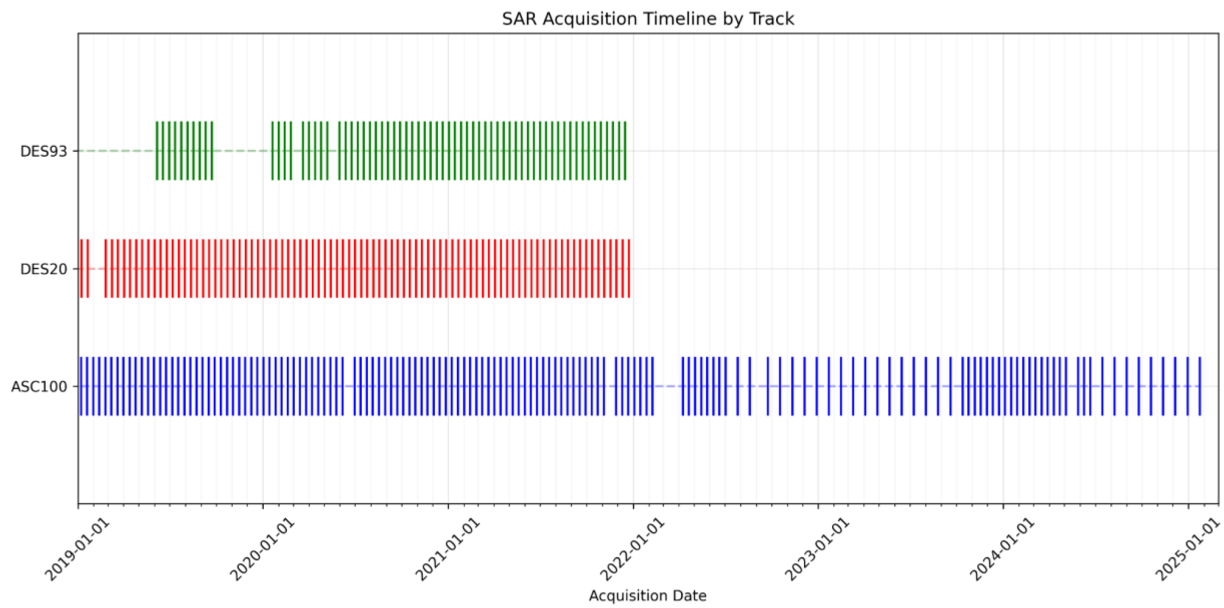

Figure 19 - Timeline of Sentinel-1 SAR acquisitions over the FORGE area.

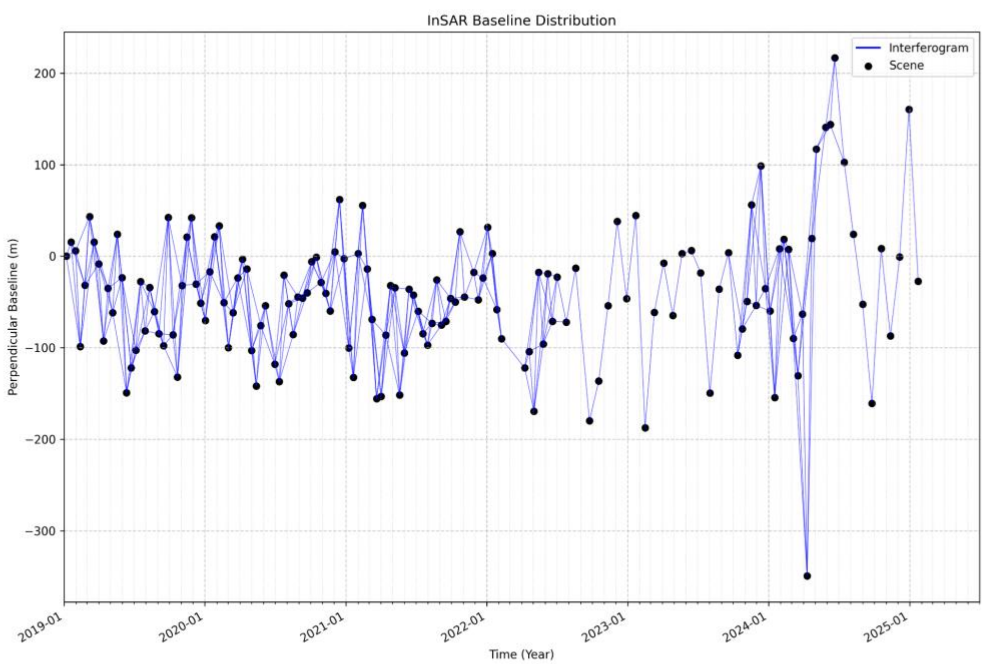

Figure 20 - Baseline distribution of the Track ASC100. Black dots represent the SAR acquisitions, and blue lines represent the interferograms used to construct the surface displacement time series.

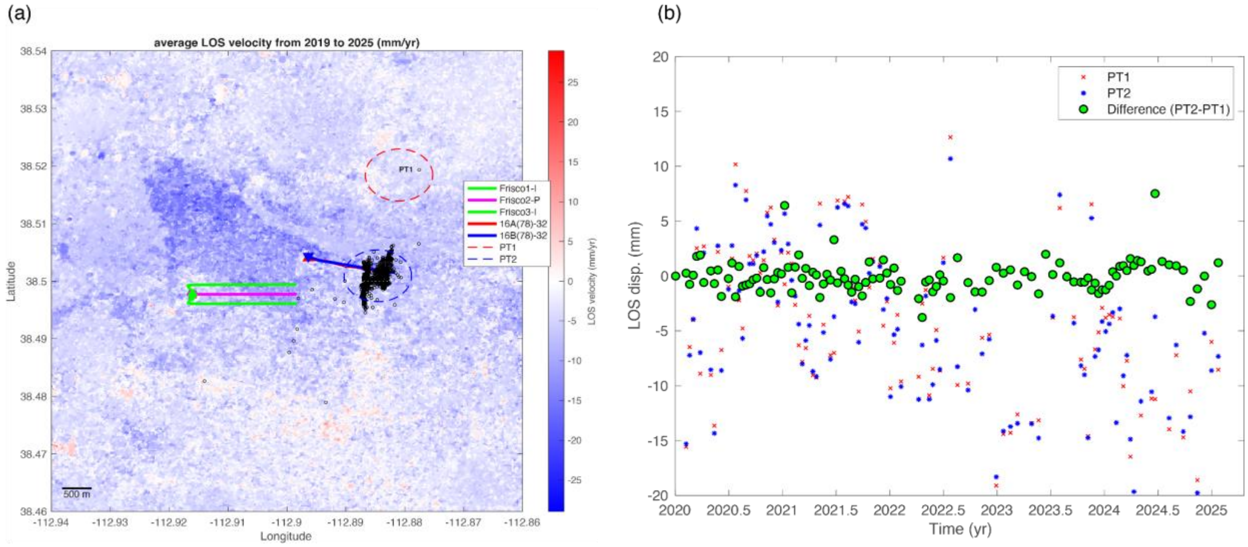

Figure 21 - (a) Average line-of-sight (LOS) velocity map over the FORGE site derived from Sentinel-1 InSAR data from 2019 to 2025 along the ascending track ASC100. Two 500-meter radius circles are overlaid on the map: one centered on the ends of wells 16A and 16B to approximate the extent of the microseismicity cluster (Niemz et al., 2025), and a reference point located approximately 1 km north of the cluster. LOS displacement time series within the circles, and their difference, are shown in (b).

III. Conclusions and Future Work

Our examination of the Distributed Strain Sensing (DSS) data from the April 2024 stimulations at the FORGE site indicates that the observations are of sufficient quality for both the forward and inverse modeling proposed in this project. Furthermore, the general correlation between seismicity and DSS observations is promising and suggests that a joint quantitative interpretation is indeed feasible.

Although the current Sentinel-1 InSAR analysis does not reveal clear surface deformation signals during the recent stimulation tests, it does not rule out the possibility of minor, localized deformation below the InSAR detection threshold. As noted in previous reports, SAR data from other missions, such as the X-band TerraSAR-X (TSX) and the upcoming L-band NISAR, may offer higher sensitivity to subtle surface displacement and provide complementary insights into the subsurface dynamics associated with the stimulations.

References

Feigl, M. and Batzli, 2024. Report and associated data from measuring and modeling deformation 2018 through 2024. *Utah FORGE Report 1621*, https://gdr.openei.org/submissions/1621.

Masson, Y., J. and Pride, S. R., 2010. Finite-difference modeling of Biot's poroelastic equations across all frequencies, *Geophysics*, **75**, N33-N41.

Niemz, P., Pankow, K., Isken, M. P., Whidden, K., McLennan, J., and Moore, J., 2025. Mapping fracture zones with nodal geophone patches: Insights from induced microseismicity during the 2024 stimulations at Utah, FORGE, *Seismological Research Letters*, 1-16, doi: 10.1785/0220240300.

Tymofyeyeva, E., & Fialko, Y., 2015. Mitigation of atmospheric phase delays in InSAR data, with application to the eastern California shear zone. *Journal of Geophysical Research: Solid Earth*, 120(8), 5952–5963. doi:10.1002/2015jb011886

Vasco, D. W., Smith, J. T., and Hoversten, G. M., 2020. Seismicity and stress associated with a fluid-driven fracture: Estimating the evolving geometry, *Journal of Geophysical Research*, **125**, doi.org/10.1022/2020JB020190.

Wang, K., Dreger, D. S., Burgmann, R., & Taira, T., 2023. Finite-Source Model of the 8 July 2021 M 6.0 Antelope Valley, California, Earthquake. *Seismological Research Letters*. doi:10.1785/0220220262